

Article

Disinfection and Photocatalytic Degradation of Organic Contaminants Using Visible Light-Activated GCN/Ag₂CrO₄ Nanocomposites

Olufemi Oluseun Akintunde ¹, Linlong Yu ¹, Jinguang Hu ², Md Golam Kibria ², Casey R. J. Hubert ³, Samuel Pogolian ⁴ and Gopal Achari ^{1,*}

¹ Department of Civil Engineering, University of Calgary, ENE 231, 2500 University Drive NW, Calgary, AB T2N 1N4, Canada

² Department of Chemical and Petroleum Engineering, University of Calgary, ENB 202, 2500 University Drive NW, Calgary, AB T2N 1N4, Canada

³ Department of Biological Sciences, University of Calgary, Biological Sciences 186, 2500 University Drive NW, Calgary, AB T2N 1N4, Canada

⁴ Nemalux Industrial, 1018 72 Ave NE, Calgary, AB T2E 8V9, Canada

* Correspondence: gachari@ucalgary.ca

Abstract: Visible-light-driven photocatalysts have gained increasing attention in the past few decades in treating emerging contaminants in water and wastewater. In this work, the photocatalytic activity of the coupled graphitic carbon nitride (GCN) and silver chromate (Ag₂CrO₄), herein denoted as GCN/Ag₂CrO₄, nanocomposites was evaluated for degrading organic pollutants and inactivating microorganisms under visible light irradiation using a royal blue light-emitting diode (LED). The organic pollutants studied were 2,4-dichlorophenoxyacetic acid (2,4-D) and methyl chlorophenoxy propionic acid (MCP or Mecoprop-P) present in Killlex^R, a commercially available herbicide, bovine serum albumin (BSA) protein, and SARS-CoV-2 spike protein. The disinfection experiments were conducted on wastewater secondary effluent. The results showed that over 85% degradation was achieved for both 2,4-D and Mecoprop-P in 120 min while 100% of BSA protein and 77.5% of SARS-CoV-2 protein were degraded in 20 min and 30 min, respectively. Additionally, GCN/Ag₂CrO₄ nanocomposites led to over one log reduction of cellular ATP (*cATP*), total coliforms, and *E. coli* in wastewater treatment plant (WWTP) secondary effluent after 60 min of royal blue LED irradiation. It was observed that the degradation performance of a photocatalyst under light irradiation is contaminant-specific. The binding affinity of the released metal ions from GCN/Ag₂CrO₄ with protein and ATP functional groups was responsible for the degradation of proteins and the reduction of *cATP*, while the generated ROS was responsible for the disinfection of total coliforms and *E. coli*. Overall, the results indicate that GCN/Ag₂CrO₄ nanocomposite is a promising photocatalyst in degrading organic pollutants and disinfecting microorganisms under visible light irradiation within a reasonable time.

Keywords: GCN/Ag₂CrO₄; photocatalysis; organic pollutants; microorganisms; wastewater; royal blue LED



Citation: Akintunde, O.O.; Yu, L.; Hu, J.; Kibria, M.G.; Hubert, C.R.J.; Pogolian, S.; Achari, G. Disinfection and Photocatalytic Degradation of Organic Contaminants Using Visible Light-Activated GCN/Ag₂CrO₄ Nanocomposites. *Catalysts* **2022**, *12*, 943. <https://doi.org/10.3390/catal12090943>

Academic Editors: Jorge Bedia and Carolina Belver

Received: 6 August 2022

Accepted: 21 August 2022

Published: 25 August 2022

Publisher's Note: MDPI stays neutral with regard to jurisdictional claims in published maps and institutional affiliations.



Copyright: © 2022 by the authors. Licensee MDPI, Basel, Switzerland. This article is an open access article distributed under the terms and conditions of the Creative Commons Attribution (CC BY) license (<https://creativecommons.org/licenses/by/4.0/>).

1. Introduction

Semiconductor photocatalysis is fast emerging as the advanced oxidation process to address environmental pollution and global warming such as organic pollutant removal, disinfection of microorganisms, hydrogen evolution, and CO₂ reduction [1–5]. In semiconductor photocatalysis, photoexcited electrons and holes are generated when the energy absorbed from light is greater than or equal to the bandgap energy of the photocatalysts. These electrons react with the dissolved oxygen in the solution while the holes react with water molecules to produce superoxide radical (O₂^{•−}) and hydroxyl radical (•OH), respectively. These radicals are referred to as reaction oxidative species (ROS) and they can

oxidize organic pollutants, finally producing mineralized products such as CO₂ and H₂O. They can also be used for disinfection purposes. Titanium dioxide (TiO₂), a metal-based semiconductor, is the most widely studied photocatalyst, but it suffers from limited applications such as wide bandgap (3.2 eV), low visible light utilization, and high recombination rate of electron-hole pair [6–9]. Therefore, various semiconductor photocatalysts with narrow bandgap and visible-light activity were developed such as Bi₂WO₆ [10], CuO [11], and CdS [12]. To this end, modified and doped TiO₂ [13], photosensitizers [14], as well as the use of low-energy systems such as light-emitting diodes [15,16] and “adsorb and shuttle” wherein adsorbent along with a photocatalyst [17] have also been investigated.

Graphitic carbon nitride (g-C₃N₄ or GCN) is a metal-free photocatalyst, with a bandgap of 2.7 eV that has gained a lot of attention in photocatalytic water splitting [18], photocatalytic degradation of organic pollutants [19], and disinfection of microorganisms [20] under visible light irradiation [21,22]. However, the major drawback of bulk GCN is low surface area, high rate of electron-hole pair recombination, and low utilization of visible light up to only 460 nm (blue region) which limits its photocatalytic activity [23].

It is well known that silver-based photocatalysts such as silver halides [24,25], Ag₃PO₄ [26], and Ag₂CrO₄ [27] are potential catalysts because of their excellent light sensitivity and photocatalytic activity under visible light irradiation. Of note is Ag₂CrO₄ with its high visible-light absorption efficiency, and electronic and crystal structure [28]. However, Ag₂CrO₄, like other silver-based photocatalysts, has similar drawbacks which are aggregated particle size and ease of photocorrosion leading to poor stability and limited photocatalytic performance.

Coupling of GCN and the silver-based photocatalysts to form heterojunctions can address the individual shortcomings of GCN and silver-based photocatalysts by improving charge separation, reducing the rate of recombination of electron-hole pair, improving bandgap optical properties, and enhancing visible light absorption and utilization of GCN, as well as reducing the aggregation of silver-based photocatalysts. For example, GCN/Ag [23], GCN/AgBr [29], GCN/Ag₃PO₄ [30], and GCN/Ag₂CrO₄ [31] showed higher degradation of methylene blue (MB), *E. coli* disinfection, 4-chlorophenol (4-CP) degradation, and methyl orange (MO) degradation, respectively, under visible light when compared to GCN.

The purpose of this study is to investigate synthesized GCN/Ag₂CrO₄ to photocatalytically degrade organic pollutants as well as disinfect microorganisms. Killex^R (2,4-D and Mecoprop-P), BSA, and SARS-CoV-2 spike protein were selected to study while WWTP secondary effluent was used to assess photocatalytic disinfection. The addition of Ag₂CrO₄ to GCN to form the GCN/Ag₂CrO₄ heterojunction enhances visible-light activity. Ag₂CrO₄ being a strong oxidizing agent serves as electron trap by accepting photogenerated electrons from GCN thereby reducing electron-hole pair recombination rate and improving charge separation. The narrow band gap of Ag₂CrO₄ (1.80 eV) indicates strong absorption in the visible-light region which could enhance its photocatalytic activity. Both 2,4-D and certain microbial constituents in wastewater such as *E. coli* have known negative health and environmental impacts [32,33]. Moreover, 2,4-D and Mecoprop-P are common constituents of herbicides that can be found on the surface and in groundwater because of their use in lawns and agricultural lands [34]. A study in Alberta, Canada showed that 2,4-D is one of the most common pollutants in water and precipitate samples [35]. Mecoprop-P has been detected as a minor pollutant in U.S. and European soils, as well as in ground and surface waters, and it is the most often found herbicide in drinking waters [36,37]. Bovine serum albumin protein (BSA) is a commonly used standard for protein analysis selected for studying the interaction between proteins and other chemicals. SARS-CoV-2, the Coronavirus that causes COVID-19, has resulted in a worldwide pandemic with over 280 million infections and caused over 5 million deaths globally [38]. This viral disease continues to ravage the world with severe or mild variants. COVID-19 burden in communities has been monitored by testing wastewater to provide an early warning of a community spread [39]. Sources of coliforms can be humans, livestock, wildlife, and even pets. *E. coli* is considered

a potential pathogen and its presence in the water body can indicate the presence of other waterborne pathogens such as bacteria, viruses, and parasites [40].

Photocatalytic degradation of 2,4-D and Killex using TiO_2 has been widely reported [41–43]. However, only a few studies focused on the photocatalytic degradation of 2,4-D using GCN. The degradation of 2,4-D using GCN-based composite under natural sunlight showed over 90% removal after 330 min [44]. About 100% degradation of a very small concentration (50 $\mu\text{g/L}$) of Mecoprop-P was achieved in 7 min using a GCN-based catalyst under simulated solar irradiation [45]. Heydari et al. degraded Killex^R (2,4-D and Mecoprop-P) using TiO_2 under natural sunlight exposure with 97% degradation of 2,4-D after 15 days and 100% degradation of Mecoprop-P after 22 days [46]. The enhancement of the photocatalytic activity of GCN in degrading methylene blue (MB) was achieved with its combination with Co-NiS and sulfur to form 1D/2D Co-NiS/S-g- C_3N_4 heterojunction with 98% degradation in 32 min [47]. $\text{ZnFe}_2\text{O}_4/\text{S-g-C}_3\text{N}_4$ heterojunction was synthesized with varying wt% of S-g- C_3N_4 . The $\text{ZnFe}_2\text{O}_4/\text{S-g-C}_3\text{N}_4$ (50%) showed the maximum MB degradation under solar irradiation in 150 min [48]. The interaction between BSA and nanoparticles and the structural change to BSA have been investigated with nanoparticles such as MnO_2 [49], CuS [50], and silver nanoparticles (AgNP) [51,52] at different concentrations and compositions. The results show increasing interactions and structural changes to BSA with increasing concentration of the nanoparticles. The disinfection of *E. coli* using GCN-based composite under a xenon lamp as a solar simulator showed complete inactivation (6.5 log) after 60 min [29]. In the published literature, the focus was on either natural sunlight or solar simulator as broadband light source for the photocatalytic degradation and disinfection. To the best of our knowledge, the combination of a narrowband low-energy visible light source (in this case royal blue LED with a peak wavelength of 460 nm) and GCN-based nanocomposites has not been reported on degrading herbicides and protein and disinfecting WWTP secondary effluent. The benefits of narrowband light are its consistency, directionality (narrow and focused beam), and narrow frequency range [53]. The photons in narrowband light move at the same wavelength (consistency) and in the same direction (directionality) resulting in high light intensity.

This work aims to address the knowledge gaps in evaluating the photocatalytic performance of GCN/ Ag_2CrO_4 nanocomposite under a narrowband low-energy visible light source (royal blue LED) in degrading different organic pollutants such as Killex^R (2,4-D and MCP), BSA protein, SARS-CoV-2 spike protein, and disinfecting WWTP secondary effluent. The reaction kinetics of 2,4-D, Mecoprop-P, and BSA protein were also investigated. The interaction between BSA and the photocatalysts, and the structural changes to BSA were studied using a UV-Vis spectrophotometer; log reduction of cellular ATP (cATP), total coliforms, and *E. coli* in WWTP secondary effluent was used to determine the efficiency of the catalyst in wastewater disinfection.

2. Results and Discussions

2.1. Photocatalytic Degradation of Killex^R

The dark adsorption of 2,4-D and Mecoprop-P on the synthesized photocatalyst are presented in Figure 1. It is obvious that GCN alone did not adsorb and thus there was no decrease in the concentration of 2,4-D or Mecoprop-P during the dark experiment. Equilibrium was reached within 30 min for Ag_2CrO_4 and GCN/ Ag_2CrO_4 . A total of 8.06% of 2,4-D was adsorbed on Ag_2CrO_4 while 9.32% of Mecoprop-P was adsorbed on Ag_2CrO_4 . A total of 6.24% of 2,4-D was adsorbed on GCN/ Ag_2CrO_4 while 15.32% of Mecoprop-P was adsorbed on GCN/ Ag_2CrO_4 . The photocatalytic degradation of GCN/ Ag_2CrO_4 on the 2,4-D and Mecoprop-P in Killex^R was investigated and the results are presented in Figure 2. In the control experiment, 2,4-D and Mecoprop-P did not decrease with irradiation by royal blue LED, indicating that the royal blue light (peak wavelength = 460 nm) did not degrade 2,4-D or Mecoprop-P. Using GCN, 16.85% of 2,4-D and 10.06% of Mecoprop-P degraded after 120 min. Ag_2CrO_4 remains largely unchanged under royal blue LED irradiation when compared to the dark experiment results. It was 7.05% for 2,4-D and 9.19% for Mecoprop-

P. This is because silver-based photocatalysts are prone to photolysis and cannot stand long-run duration of photocatalytic degradation [30], and the low surface area of Ag_2CrO_4 ($1.32 \text{ m}^2/\text{g}$) [21] available for the adsorption of 2,4-D and Mecoprop-P and the eventual photocatalytic activity. Silver-based particles have been reported to aggregate [54] while GCN in the GCN/ Ag_2CrO_4 nanocomposite serves to prevent the aggregation of Ag_2CrO_4 . GCN/ Ag_2CrO_4 showed the highest percent degradation for both 2,4-D and Mecoprop-P at 86.32% and 86.39% in 120 min.

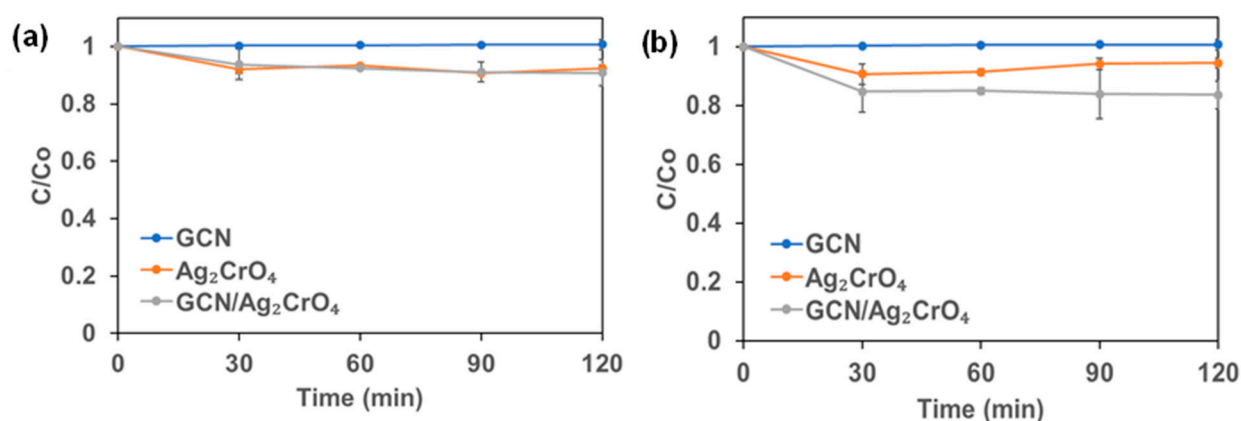


Figure 1. The dark experiment of Killlex^R: (a) 2,4-D and (b) Mecoprop-P.

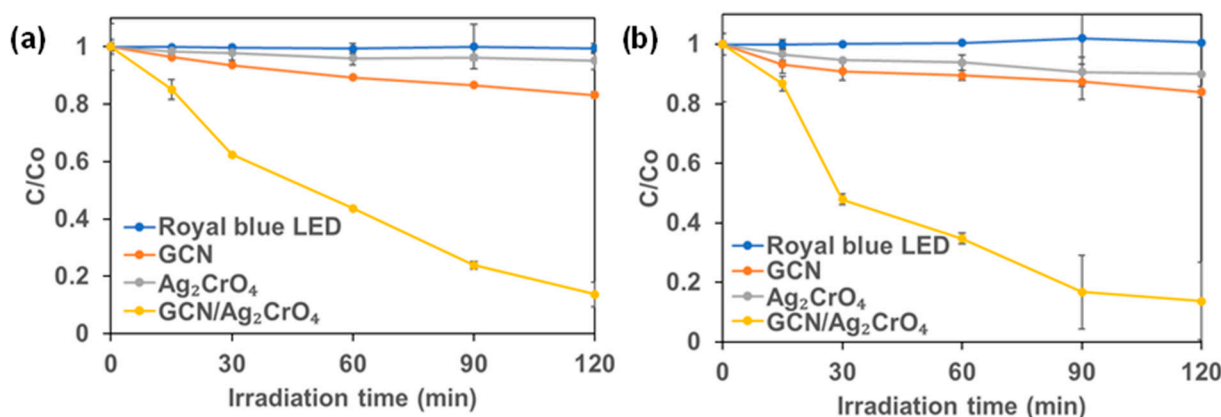


Figure 2. Photocatalytic degradation (royal blue LED irradiation) of Killlex^R: (a) 2,4-D and (b) Mecoprop-P.

The first-order rate was calculated to evaluate the performance of the different photocatalysts. The rate constant (k) values are summarized in Table 1. For 2,4-D, the k values of GCN and GCN/ Ag_2CrO_4 were $0.16 \times 10^{-2} \text{ min}^{-1}$ and $1.59 \times 10^{-2} \text{ min}^{-1}$ respectively. The highest k value for degradation using GCN/ Ag_2CrO_4 was 9.9 times that with GCN alone. For Mecoprop-P, the k values of GCN and GCN/ Ag_2CrO_4 were $0.11 \times 10^{-2} \text{ min}^{-1}$ and $1.79 \times 10^{-2} \text{ min}^{-1}$ respectively. The highest k value for the photocatalyst GCN/ Ag_2CrO_4 was $1.79 \times 10^{-2} \text{ min}^{-1}$ which was 16.3 times that of GCN. This result shows that the deposition of Ag_2CrO_4 on GCN enhanced its photocatalytic activity by serving as an electron trap for photogenerated electrons in GCN.

Table 1. Summary of first-order photocatalytic degradation rate constants.

Experimental Condition		GCN	Ag ₂ CrO ₄	GCN/Ag ₂ CrO ₄
2,4-D	Rate constant, k ($\times 10^{-2}$) min ⁻¹	0.16	1.20	1.59
	R ²	0.9891	0.6227	0.9959
Mecoprop-P	Rate constant, k ($\times 10^{-2}$) min ⁻¹	0.11	1.26	1.79
	R ²	0.8167	0.6377	0.9874

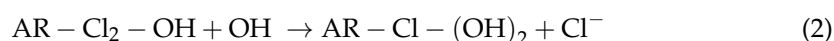
In our previous publication, we reported that the photocatalytic degradation of 4-CP by GCN/Ag₂CrO₄ was better than GCN [21], while in this study (Figure 2a,b) we find a better performance was observed for GCN than Ag₂CrO₄ in the photocatalytic degradation of 2,4-D and Mecoprop-P. This indicates that the photocatalytic degradation performance of Ag₂CrO₄ is contaminant-specific. This can be attributed to the bond energies existing in the contaminants such as C-C, C=C, O-H, C=O, and C-Cl. Bond energy or bond dissociation energy is the measure of bond strength, and it is an indication of the easiness to break a chemical bond. The bond energies of bonds existing in 4-CP, 2,4-D, and Mecoprop-P are shown in Table 2.

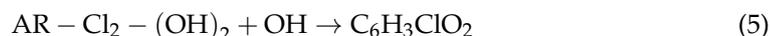
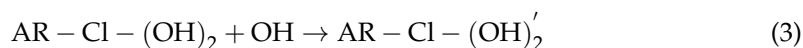
Table 2. Bond energies at 273K adapted from Ref. [55].

Bond	Bond Energy (KJ/mol)
C-Cl	327
C-C	346
C-O	358
C-H	411
O-H	459
C=C	602
C=O	749

There are fewer bonds in 4-CP than 2,4-D and Mecoprop-P that need to be broken by ROS generated from Ag₂CrO₄. In 4-CP, apart from the aromatic ring, there are C-Cl, C-O, and O-H corresponding to 327 KJ/mol, 358 KJ/mol, and 459 KJ/mol, while 2,4-D and Mecoprop-P have all the bonds listed in Table 2 in addition to the aromatic ring. This means with 2,4-D and Mecoprop-P having more bonds and higher bond energies, they will be more difficult to break by the ROS generated from Ag₂CrO₄ and hence the observed low photocatalytic performance compared to 4-CP. The low surface area of Ag₂CrO₄, in addition to the bond energies of the contaminants, also would have contributed to the low performance. With a specific surface area of 1.32 m²/g [21], it means that less absorption of 2,4-D and Mecoprop-P would take place for sufficient photocatalytic activity compared to single contaminant absorption of 4-CP. Therefore, the combination of the low surface area of Ag₂CrO₄ for the absorption of the two contaminants and the several bonds and higher bond energies of 2,4-D and Mecoprop-P contributed to the observed low performance of Ag₂CrO₄.

In the photocatalytic degradation of pollutants, the molecular structures could determine their susceptibility to ROS attack [45]. The compounds 2,4-D and Mecoprop-P are both chlorophenoxy herbicides (phenoxycarboxylic acid herbicides). These similar structures could explain their similar degradation rates under visible light. In the photocatalytic degradation of 2,4-D, the aromatic ring of 2,4-D is first hydroxylated to the main by-product, 2,4 dichlorophenol (2,4-DCP), followed by other by-products such as chlorohydroquinone, 4-chloropyrocatechol, 2,4-dichloropyrocatechol, and chlorobenzoquinone [56,57] as shown in Equations (1)–(5), where AR is the aromatic ring.





In addition, in the photocatalytic degradation of Mecoprop-P, the aromatic ring is hydroxylated to the main by-product, 4-chloro-o-cresol, followed by other by-products such as 2-methyl hydroquinone, and 2-methyl-p-benzoquinone [37] as proposed in Equations (6)–(8). The main reactive species involved in photocatalytic degradation is the $\bullet\text{OH}$ radical as reported for 2,4-D [44,58–60] and Mecoprop-P [45,61]. Table 3 shows the photocatalytic degradation of 2,4-D and Mecoprop-P by different photocatalysts.

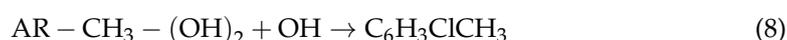


Table 3. Comparison of 2,4-D and Mecoprop-P degradation with the results of previously published articles.

S/N	Photocatalyst	Visible Light Source	Organic Pollutant	Concentration (mg/L)	Degradation Time (min)	Degradation Efficiency (%)	Ref.
1	TiO ₂	Natural sunlight	2,4-D and Mecoprop-P	49.4 and 27.3	1,296,000 and 1,900,800	97 and 100	[46]
2	MoO ₃ /g-C ₃ N ₄	Natural sunlight	2,4-D	50	300	99	[44]
3	GCN	Xenon lamp (200–800 nm, 300 W)	Mecoprop-P	0.05	7	100	[45]
4	GCN/Ag ₂ CrO ₄	Royal blue LED (460 nm)	2,4-D and Mecoprop-P	12.1 and 6.7	120 and 120	86.32 and 86.39	Current study

2.2. Photocatalytic Degradation of BSA Protein and SARS-CoV-2 Spike Protein

The interaction between the synthesized photocatalysts and BSA in the absence of light (dark experiment) was investigated and the results are shown in Figure 3a. It was observed that the concentration of BSA did not change when GCN was present in the solution, indicating that the GCN had a negligible impact in the dark experiment. However, it was observed that the concentration of BSA decreased significantly by 93.1% in 30 min in the presence of GCN/Ag₂CrO₄. The photocatalytic degradation results of BSA are presented in Figure 3b. It shows that royal blue LED irradiation alone and GCN/royal blue LED irradiation could not degrade BSA. The royal blue LED with peak wavelength of 460 nm and low energy (2.7 eV) cannot alone degrade BSA with absorption peak of 280 nm and high energy (4.4 eV) indicating that BSA requires high energy radiation greater than 4.4 eV for degradation to take place. The GCN/royal blue LED could not degrade BSA because of the high electron-hole pair recombination rate of GCN owing to its medium band gap (2.7 eV). However, more than 99.9% of BSA was degraded in 20 min in the presence of GCN/Ag₂CrO₄ under royal blue LED irradiation. The first-order rate constant (k) values of GCN and GCN/Ag₂CrO₄ were calculated, and they are $0.002 \times 10^{-1} \text{ min}^{-1}$ and $3.64 \times 10^{-1} \text{ min}^{-1}$ respectively.

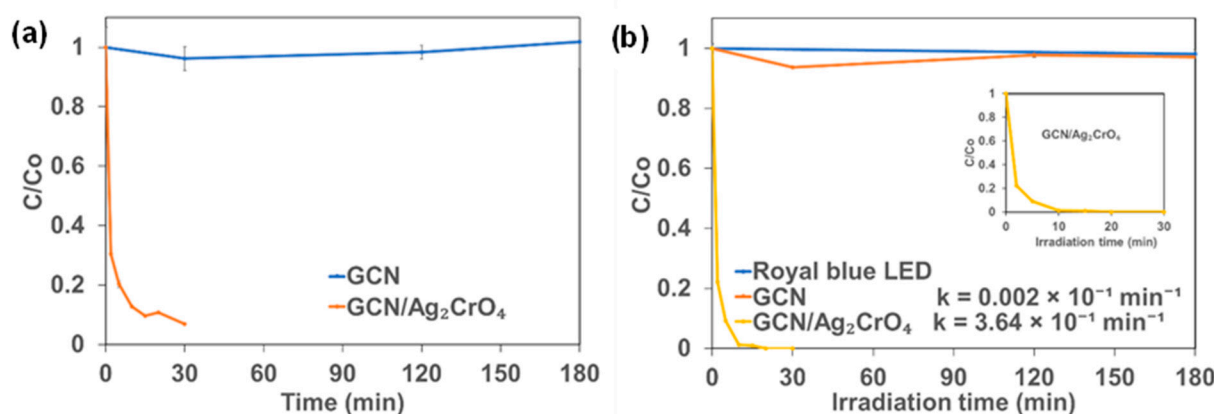


Figure 3. Change in BSA concentration with time: (a) Dark experiment and (b) Royal blue LED irradiation.

In a recently published work, the photocatalytic degradation mechanism of protein using silver nanoparticles (AgNPs) was reported by investigating the effects of the following 3-step phenomenon; release of silver ions, generation of reactive oxidative species (ROS), and the light-induced protein oxidation through the bind-and-damage model [62]. It was postulated and concluded by asserting an alternate mechanism, which is that light-induced protein oxidation is responsible for the degradation rather than the popular notions that the mechanisms of Ag^+ release from AgNPs and the generation of ROS are the driving forces for protein degradation and bacterial death. For the bind-and-damage model of the light-induced protein oxidation to take place, the AgNPs released the absorbed visible light energy in the form of emission. This emission of light is then quenched by a protein which indicates that the absorbed light energy was transferred to the protein, causing structural damage to the proteins.

The assertions were applied to this work for verification by carrying out UV-vis absorption spectra measurements of BSA for GCN and GCN/Ag₂CrO₄ with and without royal blue LED irradiation to further understand the degradation profile and the change in concentration with time. UV-vis, as an analytical method, can be used in absorption spectra measurement in understanding structural changes to protein and the interaction between protein and nanoparticles [49,50,63,64]. The observation was that the phenomena: release of Ag^+ from the Ag₂CrO₄, generation of ROS through photocatalytic reaction, and the bind-and-damage model of the light-induced protein oxidation, have varying degrees of contribution to the degradation of protein in the presence of GCN/Ag₂CrO₄ with and without blue LED irradiation. The roles these phenomena play in either protein degradation or bacterial death will depend on the type of photocatalyst, light intensity, radiation spectrum, and energy of the light source. In this work, two ions (Ag^+ and CrO_4^{2-}) were released against Ag^+ of AgNPs since GCN/Ag₂CrO₄ composite was used, indicating the possibility of the impact of CrO_4^{2-} in the degradation mechanism as an electron scavenger during photocatalytic activity. The UV-vis absorption spectrum in Figure 4 shows the effect of GCN and GCN/Ag₂CrO₄ on BSA with and without royal blue LED irradiation. At time zero (Figure 4a–d), BSA shows the typical absorption peaks at a lower wavelength of 200 nm and a higher wavelength of 280 nm. The absorption peak at 200 nm is attributed to the BSA's polypeptide backbone and the absorption peak at 280 nm is due to its aromatic amino acids (tryptophan, tyrosine, and phenylalanine). In Figure 4a,c, the GCN without and with royal blue LED irradiation revealed similar absorption spectra. In Figure 4a, without light (dark), the BSA peak did not change because the conditions required for protein damage which are light-induced protein oxidation and ROS generation are not present since photocatalytic activity did not take place. It also indicates no interaction between the BSA and GCN, hence no structural change to the protein. In Figure 4c, under royal blue LED irradiation, the bind-and-damage model of the light-induced protein oxidation and

the generated ROS did not have an impact on the degradation of the protein. This suggests that the emitted light from the absorbed light energy by the GCN was neither sufficient nor transferred to the protein for degradation, and the generated ROS was not sufficient to cause degradation because of the GCN's poor charge transfer and fast electron-hole recombination rate characteristics. In the presence of GCN/Ag₂CrO₄ (Figure 4b,d), an absorption peak at 374 nm was observed. This peak is attributed to the presence of silver chromate in the BSA slurry. Silver compounds are known to have absorption peaks between 320 nm and 410 nm [51,52,65]. In Figure 4b,d, the GCN/Ag₂CrO₄ without and with royal blue LED irradiation show similar spectral patterns. In Figure 4b, without light (dark), Ag⁺ and CrO₄²⁻ were released by Ag₂CrO₄ in the GCN/Ag₂CrO₄ nanocomposite. The interactions of the Ag⁺ with BSA resulted in higher BSA absorption peaks compared to GCN without light (dark). In Figure 4d, under royal blue LED irradiation the bind-and-damage model light-induced protein oxidation and the ROS generation did not significantly contribute to the protein degradation since the peaks without light and with royal blue LED are similar. This is evident in the change in BSA concentration when exposed to GCN/Ag₂CrO₄ with and without royal blue LED irradiation (Figure 3a,b), where the degradation is similar at 90% and 99% in 15 min respectively. Therefore, we can conclude the following: (1) the Ag⁺ released from GCN/Ag₂CrO₄ was largely responsible for BSA protein degradation with and without royal blue LED irradiation, and (2) the bind-and-damage model of light-induced protein oxidation and the generation of ROS did not significantly contribute to photocatalytic degradation of BSA protein, indicating that the light irradiation had less impact in the photocatalytic process. The less impact of light irradiation is expressed in the proximities of the degradation kinetics of GCN/Ag₂CrO₄ with royal blue irradiation ($3.64 \times 10^{-1} \text{ min}^{-1}$) which is less than two times without light, that is dark ($1.86 \times 10^{-1} \text{ min}^{-1}$). The reason for the dominance of these silver ions in the degradation of BSA protein could be attributed to their binding interactions with BSA. Previous studies show that silver ions and silver nanoparticles interact with protein functional groups, such as carboxylic groups (COOH), thiol groups (SH), and amino groups (NH) of protein, to form bonds resulting in protein inactivation [51,66–69]. Zaher et al. investigated the interaction between Ag⁺ and AgNPs with BSA protein and reported that Ag⁺ has stronger binding and quenching efficiency towards BSA than AgNPs which is evidenced in a higher binding constant of Ag⁺ [70]. BSA is a polymer of about 583 amino acids joined together by peptide linkage between two tryptophan residues. Each amino acid has two pH-sensitive functional groups, COOH and NH. The proposed binding mechanism was due to the electrostatic attraction between the ionized COO⁻ and the positive charge of Ag⁺ at physiological pH (pH = 7.4). This was confirmed in the reported UV-vis spectra showing the peak intensity increasing with rising Ag⁺ concentration. This correlates with our UV-vis spectra results for GCN/Ag₂CrO₄ with and without royal blue LED irradiation where the BSA peak intensity increases indicating a rise in Ag⁺ concentration with time in the reacting medium and therefore the increasing interaction between the COO⁻ and Ag⁺ electrostatically. This interaction leads to denaturing, unfolding, aggregation, and the eventual inactivation of the protein. Jaiswar et al. investigated the binding interaction between protein and chromate ions and reported structural changes to protein, indicating successful interactions [71].

In Figure 5, SARS-CoV-2 (Coronavirus) spike protein result is presented. It shows that GCN/Ag₂CrO₄ also can degrade the spike protein under royal blue LED. A photocatalytic degradation efficiency of 77.5% was achieved in 30 min. The lower degradation efficiency observed for SARS-CoV-2 spike protein (SP) can be attributed to its heavier molecular weight and structure. SARS-CoV-2 SP is 135 kDa and 1213 amino residues which is twice the size of BSA protein which is 66 kDa and 583 amino acid residues.

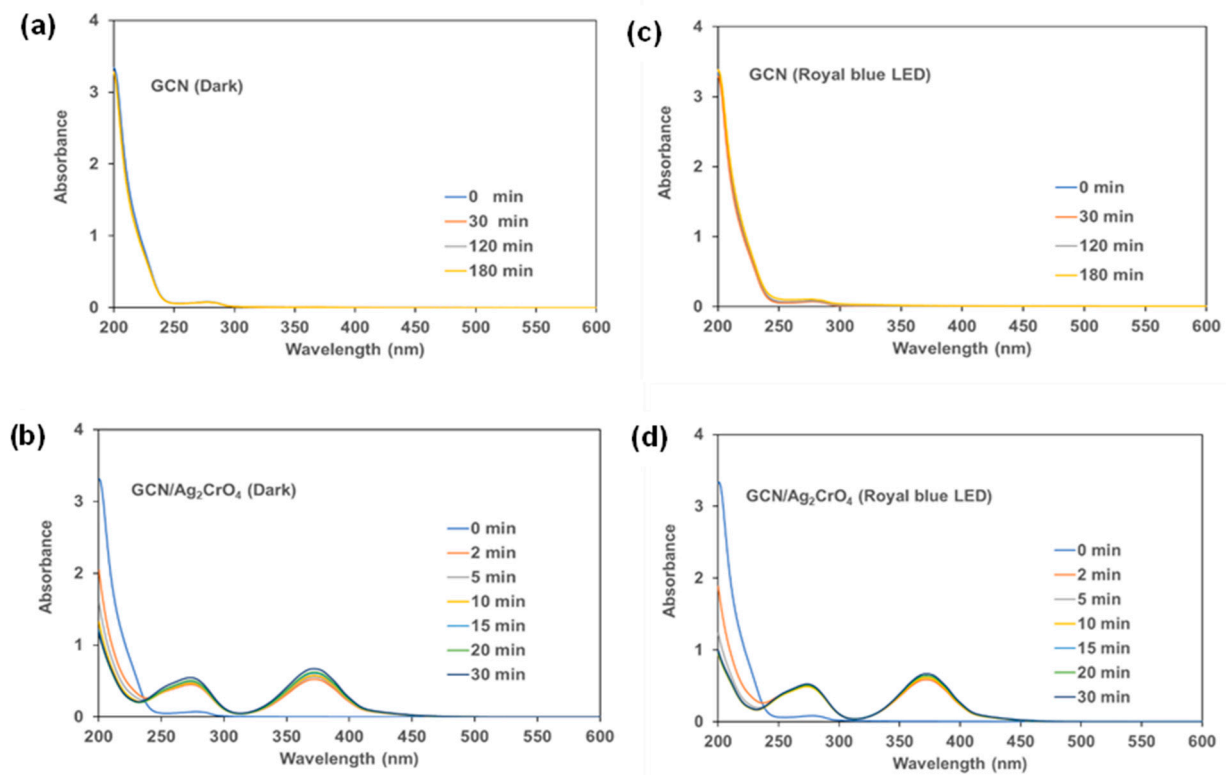


Figure 4. UV-vis absorption spectra of BSA: Dark experiment (a,b) and Royal blue LED irradiation (c,d).

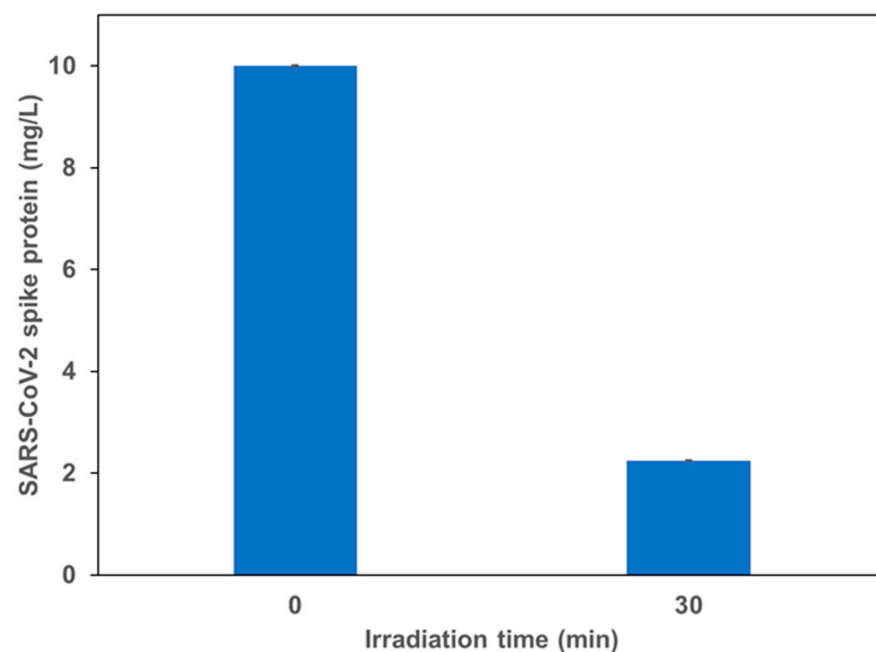


Figure 5. Photocatalytic degradation of SARS-CoV-2 (Coronavirus) spike protein using GCN/Ag₂CrO₄. Under royal blue LED irradiation.

2.3. Photocatalytic Disinfection of Wastewater Secondary Effluent

Results on the disinfection of secondary effluent from a municipal wastewater treatment plant by GCN/Ag₂CrO₄ are presented in Figures 6 and 7. The log reduction of cellular Adenosine Triphosphate (cATP) is presented in Figure 6, while the log reduction of

total coliforms and *E. coli* is presented in Figure 7. As shown in Figure 6, around 0.2 log reduction of *cATP* was observed after 60 min of royal blue LED irradiation or after 60 min of dark (control experiment). The presence of GCN/Ag₂CrO₄ in the dark or royal blue LED irradiation both increased the log reduction of *cATP* in wastewater. Moreover, 1.2 log reduction was observed for *cATP* when wastewater was mixed with GCN/Ag₂CrO₄ in the dark for 60 min. An even higher log reduction (>1.7) was observed in the presence of GCN/Ag₂CrO₄ under royal blue LED irradiation for 60 min.

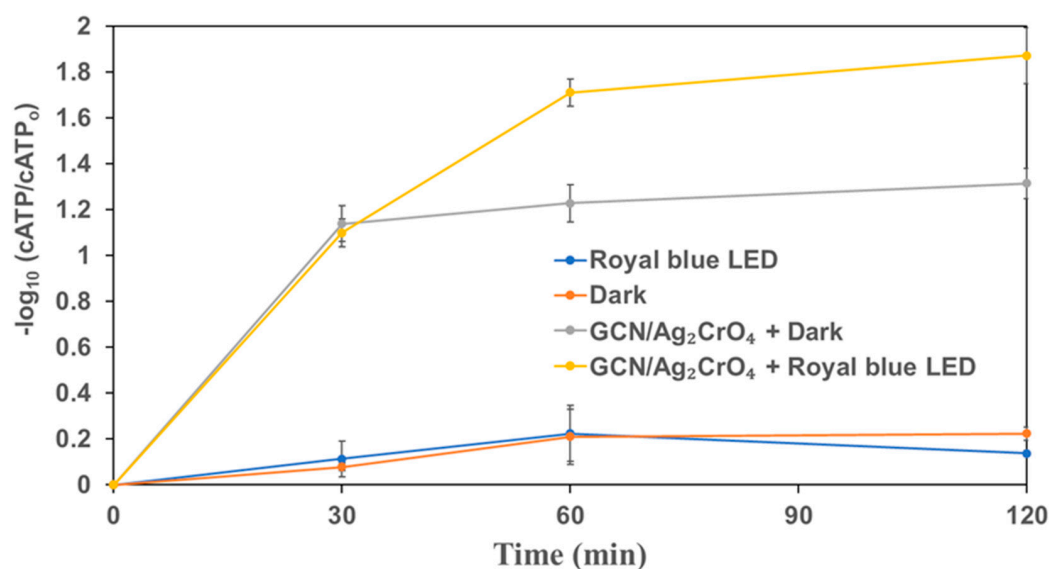


Figure 6. The change of *ATP* in wastewater secondary effluent in the presence of GCN/Ag₂CrO₄ with and without royal blue LED irradiation.

In the control experiments of royal blue LED and GCN (dark experiment), the total coliforms and *E. coli* did not decrease during the experimental duration of 60 min. This indicates that the royal blue LED irradiation and GCN (dark experiment) did not impact the total coliforms and *E. coli* counts in the wastewater. The dark control experiment of GCN/Ag₂CrO₄ and the use of GCN under royal blue LED both led to lower log reduction (<1) in 60 min for total coliforms and *E. coli*. However, the use of GCN/Ag₂CrO₄ under royal blue LED irradiation led to higher log reduction (>1) in 60 min with 2.43 log reduction of total coliforms and 1.48 log reduction of *E. coli*. This result indicates that the disinfection rate of *E. coli* was slower than that of the total coliforms.

The interaction of silver compounds with the cell membrane of the bacteria is one of the important mechanisms of silver compound toxicity [54]. This can occur both in the dark and visible light irradiation. Over one log reduction was observed for *ATP*, total coliforms, and *E. coli* in 60 min during the photocatalytic degradation process. This indicates GCN/Ag₂CrO₄ can potentially photocatalytically inactivate, under royal blue LED irradiation, over 98% (1.7 log) of the microbial activity (*ATP*) in 60 min which includes inactivation of over 99.6% (2.43 log) of total coliforms.

The bind-and-damage model of protein oxidation, release of ions from the photocatalyst, and the ROS generation processes of protein degradation described in Section 3.2 can be adopted for this disinfection process since it was used for protein degradation and bacterial disinfection by Shi et al. [62]. In Figure 6, the GCN/Ag₂CrO₄ with and without royal blue LED irradiation showed a significant impact on the reduction of *cATP* of microorganisms. Without light (GCN/Ag₂CrO₄ + Dark), the release of Ag⁺ and CrO₄²⁻ contributed to the reduction of *cATP* by 1.2 log in 60 min. However, with irradiation (GCN/Ag₂CrO₄ + Royal blue LED), the ROS generation in addition to Ag⁺ and CrO₄²⁻ released resulted in >1.7 log reduction of *cATP* in 60 min. With the marginal difference of >0.5 log reduction of *cATP*, it means the release of the two ions contributed far more than

ROS generation in the overall reduction of *cATP*. In Figure 7a, the GCN/Ag₂CrO₄ with and without royal blue LED irradiation showed a different response to the disinfection of total coliforms. Without light (GCN/Ag₂CrO₄ + Dark), the release of Ag⁺ and CrO₄²⁻ resulted in a 0.3 log reduction of total coliforms in 60 min while the irradiation (GCN/Ag₂CrO₄ + Royal blue LED), the ROS generation and the light-induced protein oxidation in addition to the released two ions resulted in 2.4 log reduction of total coliforms in 60 min. The log reduction difference >2 log is largely due to the contributions of the generated ROS and the light-induced protein oxidation. In Figure 7b, the GCN/Ag₂CrO₄, with and without royal blue LED irradiation showed a different response to *E. coli* disinfection. Without light (GCN/Ag₂CrO₄ + dark), the Ag⁺ and CrO₄²⁻ released resulted in a 0.1 log reduction of *E. coli* in 60 min while with irradiation (GCN/Ag₂CrO₄ + Royal blue LED), the generated ROS and light-induced protein oxidation in addition to the released ions resulted in 1.5 log reduction of *E. coli* in 60 min. The log reduction difference >1 log is largely due to the contributions of the ROS generated and the light-induced protein oxidation.

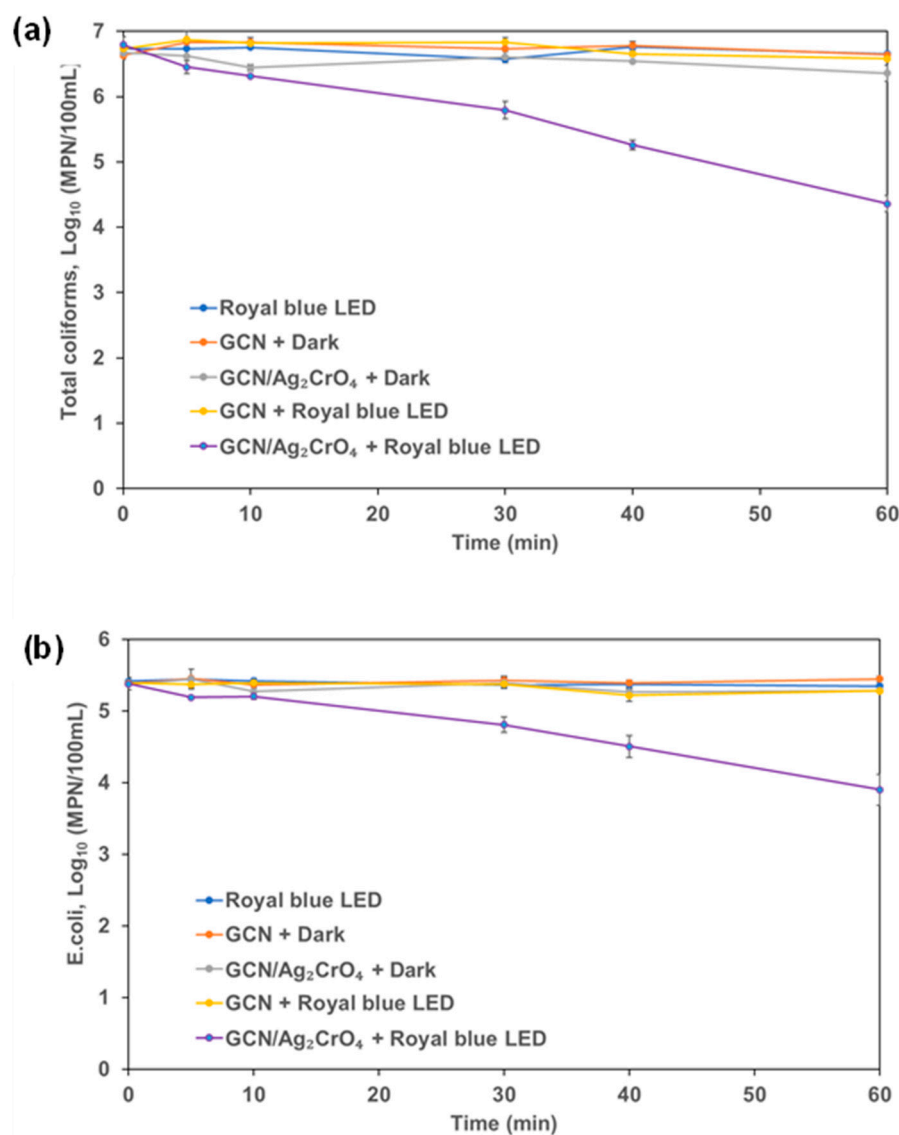


Figure 7. Coliforms in wastewater secondary effluent: (a) total coliforms and (b) *E. coli*.

Zhang et al. investigated the impact of light irradiation on the reduction of Ag⁺ to AgNPs by bacteria and reported that visible lights (monochromatic light at wavelengths 415 nm and 600 nm) accelerated the reduction of Ag⁺ to AgNPs by bacteria and almost no

AgNPs were formed in the dark [72]. Furthermore, the visible light irradiation reversibly can excite the AgNPs for their surface plasmon resonance (SPR) and accelerate the electrons from the bacteria to the adjacent Ag^+ . It reported that the bacteria can reduce Ag^+ and the process can be accelerated by light irradiation. Shi et al. focused on the bactericidal effect of AgNPs and identified a new antibacterial mechanism different from the ROS-induced photocatalyst [62]. AgNPs can penetrate the cell wall and membrane and gather in the cytosol and bind directly with the cytosol protein leading to the inducement of protein aggregation, an indication of protein degradation, caused by the bind-and-damage model of the light-induced protein oxidation. Deng et al. investigated the effects of silver ions, chromium VI, Cr(VI), and ROS on the photocatalytic disinfection mechanism of *E. coli* [29]. The results show that the combined effects of the release of silver ion and the generation of ROS of holes (h^+) and hydroxyl ($\cdot\text{OH}$) radicals played important roles in the photocatalytic disinfection process. The silver ions interact with the thiol (-SH) functional group causing cell damage and the generated ROS could inactivate bacterial cells by interacting with the cell wall and destabilizing the membrane causing leakage of potassium ions (K^+). The interaction of Ag^+ with bacterial cell membranes can also lead to lower ATP readings caused by the leakage of potassium ions [54]. The addition of hexavalent chromium to the photocatalytic system enhanced the photocatalytic disinfection kinetics. This is because Cr(VI) can behave as an electron scavenger, directly reduces electron-hole recombination, enhances the amount of h^+ available for disinfection, and ultimately leads to better disinfection performance. Table 4 shows the photocatalytic disinfection of microorganisms by different photocatalysts.

Table 4. Comparison of microorganism disinfection with the results of previously published articles.

S/N	Photocatalyst	Visible Light Source	Contaminant	Disinfection Time (min)	Concentration (CFU/mL)	Disinfection Efficiency (Log Reduction)	Ref.
1	BiOBr	Xenon lamp (1000 W/m ² , 300 W)	<i>E. coli</i>	24	10 ⁷	7	[73]
2	Ag/BiOI	Iodide lamp (400 W)	<i>E. coli</i>	20	10 ⁷	7	[74]
3	Ag/ZnO/GCN	Xenon lamp (300 W)	<i>E. coli</i>	120	10 ⁷	7	[75]
4	GCN/Ag ₂ CrO ₄	Royal blue LED (460 nm)	Total coliforms and <i>E. coli</i>	60 and 60	10 ^{6.7} and 10 ^{5.5}	2.43 and 1.48	Current study

3. Materials and Methods

3.1. Chemicals

Killex^R, a known herbicide was purchased from a local store in Calgary, Alberta. Urea-CH₄N₂O (≥99.5%), silver nitrate-AgNO₃ (≥99%), potassium chromate-K₂CrO₄ (≥99%), 1–10 phenanthroline-C₁₂H₈N₂, iron III chloride-FeCl₃, ammonium iron II sulfate hexahydrate (Mohr's salt, ≥98%)—(NH₄)₂Fe(O₄)₂(H₂O)₆ and Bovine Serum Albumin (BSA) protein (hydrolyzed powder, crystallized ≥98.0%) were purchased from Sigma-Aldrich Co. (St. Louis, MO, USA). Luria broth, potassium trioxalatoferate III trihydrate-K₃Fe(C₂O₄)₃·3H₂O (98%) was purchased from Alfa Aesar (St. Louis, MO, USA). Sodium acetate-C₂H₃NaO₂ (>99%) was purchased from Brady (Markham, ON, Canada). BSA Bradford assay protein test kit was purchased from BIORAD (Hercules, CA, USA). SARS-CoV-2 spike protein (SP), S-ECD (>95%) was purchased from Thermofisher Scientific (Ottawa, ON, Canada). ATP test kit was purchased from LuminUltra Technologies Ltd. (Fredericton, NB, Canada) while, total coliforms/*E. coli* Colilert test kit was purchased from IDEXX laboratories inc. (Westbrook, ME, USA). Secondary treated wastewater effluent was provided by Advancing Canadian Water

Assets—ACWA (Calgary, AB, Canada), a full-scale testing facility embedded in a wastewater treatment plant in Calgary, Alberta.

3.2. Preparation of GCN, Ag₂CrO₄, and GCN/Ag₂CrO₄ Nanocomposite

The GCN, Ag₂CrO₄, and GCN/Ag₂CrO₄ were synthesized based on a procedure described in detail elsewhere [21]. The GCN was synthesized using the direct pyrolysis method by heating urea at 550 °C for 4 h in a muffle furnace. The GCN/Ag₂CrO₄ composite was synthesized using the dark-induced/In-situ-deposition method by first sonicating one gram of GCN slurry. A known quantity of AgNO₃ and 4.83 g/L K₂CrO₄ were added to the GCN slurry under magnetic stirring. The mixture was then magnetically stirred in the dark for 7 h and after that, it was filtered using a 0.45 µm filter and washed about five times with water and alcohol. The residue was left to dry at room temperature and thereafter labeled as GCN/Ag₂CrO₄. The characterizations of these catalysts have been reported elsewhere [21].

3.3. Experimental Set-Up

3.3.1. Photocatalytic Degradation of a Commercial Herbicide

Killex^R is a commercially-available herbicide that contains 95 g/L of 2,4-dichlorophen oxyacetic acid (2,4-D), 52.52 g/L of methyl phenoxy propionic acid (Mecoprop-P or MCP), and 9 g/L of Dicamba. A quantity of 0.8 mL of Killex^R was dissolved in 79.2 mL of distilled water (DI) which gave an 80 mL solution, resulting in the solution containing 12.1 mg/L of 2,4-D, 6.7 mg/L of Mecoprop-P, and 1.2 mg/L of Dicamba. In this experiment, 80 mg of the photocatalyst was dispersed in an 80 mL solution containing Killex^R in a 100 mL quartz beaker. The intensity of the royal blue LED (peak wavelength = 460 nm) entering the 80 mL solution was estimated to be 11.80×10^{17} photons/s using chemical ferrioxalate actinometry [43,76,77]. The same photoreactor was used for all experiments mentioned in this study. Before LED irradiation, the water/catalysts mixture was stirred magnetically in the dark for 30 min to attain adsorption-desorption equilibrium. Quantities of 5 mL of the samples were collected at different irradiation intervals and filtered using a 0.45 µm syringe filter (PTFE, Chromatographic Specialties Inc., Brockville, ON, Canada) to remove the photocatalysts. Dark experiments with catalysts and light experiments without catalysts were also conducted as controls. HPLC was used to evaluate the concentration change of 2,4-D and Mecoprop-P.

3.3.2. Photocatalytic Degradation of BSA Protein and SARS-CoV-2 Spike Protein

In each experiment, 80 mg of the photocatalyst was dispersed in 80 mL of 100 mg/L BSA solution. During royal blue LED irradiation, 6 mL of sample was collected at different irradiation intervals and filtered using a 0.45 µm syringe filter to remove the photocatalysts. The performance of GCN/Ag₂CrO₄ was also investigated on SARS-CoV-2 spike protein (SP) under royal blue LED. In the experiment, 40 mg of the GCN/Ag₂CrO₄ was dispersed in a 40 mL of 10 mg/L SARS-CoV-2 SP, and 3 mL of the sample was collected at a different irradiation interval and filtered using a 0.45 µm syringe filter to remove the photocatalysts. Bradford assay procedure was used to determine the concentration change for the BSA protein and SARS-CoV-2 SP [78]. UV-Vis analysis was conducted for visible light and dark experiments to study the binding interaction between BSA and GCN/Ag₂CrO₄.

3.3.3. Photocatalytic Disinfection of Wastewater Secondary Effluent

Two sets of disinfection experiments were conducted. The first one was focused on the change of *cATP* level on the collected wastewater during the disinfection experiment, while the second one was aimed at quantifying the log reduction of total coliforms and *E. coli* by the catalyst under royal blue LED irradiation. For the *cATP* experiment, 80 mg of the photocatalyst was dispersed in 80 mL of wastewater secondary effluent and then irradiated with royal blue LED under continuous magnetic stirring. A total of 2.5 mL of the sample was taken at a different time interval and its *cATP* level was quantified

using the LuminUltra test procedure for assay analysis [79]. Control experiments were carried out in the dark with the photocatalyst and under the light without the photocatalyst. Before the start of the disinfection experiment, the initial concentrations of total coliforms and *E. coli* were calculated using the tray count method [80]. A stock solution of 1 L secondary treated wastewater effluent containing 50 mg of Luria broth nutrient was first prepared in a 1 L jar and then incubated at $35\text{ }^{\circ}\text{C} \pm 0.5\text{ }^{\circ}\text{C}$ for 24 h. Then 1 mL of the 80 mL collected from the stock solution was serially diluted 40 times as follows: in the first mixture, 1 mL was added to 3 mL of deionized (DI) water. After mixing, 1 mL from the first mixture was added to 9 mL of DI water to give 40 times serial dilution, this gives the second mixture. Finally, using the tray count method, 1 mL of the second mixture was added to the mixture of 100 mL DI water and colilert reagent, giving the final dilution factor of 4000. The final mixed sample was poured in a quantitray, sealed with an IDEXX sealer, and incubated at $35\text{ }^{\circ}\text{C} \pm 0.5\text{ }^{\circ}\text{C}$ for 24 h. The tray, which has 49 large wells and 48 small wells, was used to estimate the most probable number (MPN) of coliforms and *E. coli* in a 100 mL wastewater sample. The actual MPN/100 mL of total coliforms or *E. coli* present in the sample was calculated by multiplying the MPN by the dilution factor of 4000. The average initial concentrations of total coliforms and *E. coli* were calculated to be 5.2×10^6 MPN/100 mL and 0.25×10^6 MPN/100 mL respectively. Disinfection experiments were conducted and MPNs of total coliforms and *E. coli* were estimated and concentrations at different time intervals were analyzed and calculated using the tray count method. Control experiments were also performed in the dark with photocatalysts and under the light without photocatalysts.

3.4. Chemical Analysis

3.4.1. Herbicide Analysis

The concentrations of 2,4-D and Mecoprop-P were determined using high-performance liquid chromatography (HPLC; LC-2040C 3D Shimadzu Corporation, Kyoto, Japan) with UV absorbance detection at $\lambda = 280$ nm. A kinetex 2.6 μm PFP column by Phenomenex (Torrance, CA, USA) was used to separate the target compounds and other interferences. The mobile phases were 0.1% phosphoric acid in HPLC grade water and 0.1% phosphoric acid in acetonitrile at a 50:50 mixture with a flow rate of 1 mL/min. The measurements were conducted in duplicate, and the detection limit was around 0.1 mg/L.

3.4.2. Protein Analysis

The concentration of BSA protein was determined using the Bradford protein assay procedure [78]. This procedure is based on the binding of Coomassie brilliant blue dye to protein. Briefly, the diluted dye was prepared by mixing concentrated Coomassie dye (80 mL) and deionized water (DI) of 240 mL and then filtered with 5 μm using vacuum filtration to remove dye particles. From the BSA stock solution (2000 mg/L), five standard dilute solutions were prepared (100 mg/L, 50 mg/L, 25 mg/L, 12.5 mg/L and 6.25 mg/L). Then, 0.8 mL of each standard and photocatalytic degraded BSA samples were collected into the vial using a pipette and 3.2 mL of diluted dye was added. The mixture was put on a rotary shaker and left to incubate for at least 5 min but not more than 60 min at room temperature. This incubation period allows for colour change of the Coomassie dye from red to blue. This blue colour is an indication of the binding of the dye to the protein, that is detected at 595 nm. The spectrophotometer (UV-2600 Shimadzu Corp., Kyoto, Japan) was set at 595 nm to take the absorbance readings of BSA standards and the degraded samples using a disposable cuvette. The concentration of the degraded samples was calculated based on the known concentrations of the BSA standard.

This Bradford protein assay procedure was also used to determine the concentration of the SARS-CoV-2 SP. Five standard solutions of BSA of known concentrations (10 mg/L, 5 mg/L, 2.5 mg/L, and 0.625 mg/L) were prepared. Using the microassay plate, 800 μL of each standard and degraded SARS-CoV-2 SP sample was put in a vial and 200 μL of dye concentrate was added to have the protein-dye mixture. The same incubation period

as described earlier was used for the spike protein and after that, the absorbance of the SP-dye complex was read at 595 nm using a spectrophotometer (UV-2600 Shimadzu Corp., Kyoto, Japan).

The UV-vis as an analytical technique was used to study the BSA and photocatalyst interaction and the structural changes to BSA. The UV-vis absorption spectra measurements were carried out for the dark as well as royal blue irradiation samples.

3.4.3. ATP Analysis

The concentration of the microorganisms' $cATP$ was determined using the LuminUltra test kit and assay procedure [80]. A total of 5 mL of the water sample was passed through a 0.45 μm syringe filter. The syringe filter containing microorganisms was re-attached to a clean syringe with the plunger removed, and then 1 mL of UltraLyse 7 was pipette into the syringe. The filtration was done slowly, and the sample was collected in a 9 mL UltraLute (dilution) tube. The purpose of the filtration using UltraLyse 7 is to be able to dissolve and remove the bound ATP (ATP in living microorganisms after disinfection) for analysis. A quantity of 100 μL of UltraLute (dilution) solution was pipette into a clean test tube and then 100 μL Luminase was added. The mixture was shaken about five times, and then the reading was taken within 10 s using a luminometer. The cellular ATP is calculated using Equation (9) and the log reduction of the normalized concentration is evaluated using Equation (10):

$$cATP \left(\text{pg} \frac{ATP}{\text{mL}} \right) = \frac{RLU_{cATP}}{RLU_{ATP1}} \times 10,000 \frac{\text{pg} ATP}{V_{\text{sample}}(\text{mL})} \quad (9)$$

$$\text{Log reduction} = -\log \left(\frac{cATP_t}{cATP_0} \right) \quad (10)$$

where RLU is the unit of measurement as it is the relative light unit, pg is picogram, V_{sample} is the volume of the sample collected during the photocatalytic experiment, ATP is the calibrated ATP RLU value for the wastewater before the photocatalytic experiment, and $cATP_0$ and $cATP_t$ are the cellular ATP of the microorganisms at time, $t = 0$ and $t = t$ min. Control experiments were conducted in the dark to determine the adsorption performance of the photocatalysts in disinfecting microorganisms and the corresponding estimation of ATP levels.

3.4.4. Total Coliform/*E. coli* Analysis

One mL sample was collected at different irradiation intervals and serially diluted using deionized water. This was aimed to (1) reduce the amount of catalysts and other water matrices present in the final tray so as to minimize their interferences on total coliform and *E. coli* measurement; (2) to ensure the concentration of total coliform and *E. coli* fall within the measurement range of the Colilert tray count procedure. The total coliforms and *E. coli* concentrations were determined using the tray count method [80] as described in Section 3.3.3. The total coliform and *E. coli* disinfection efficiency were expressed in log form as shown in Equation (11):

$$\text{Log reduction} = \log C_0 - \log C_t \quad (11)$$

where C_0 and C_t are the concentrations of total coliforms or *E. coli* before and after time t min, expressed as MPN/100 mL.

4. Conclusions

A visible-light active photocatalyst, GCN/Ag₂CrO₄ nanocomposite was synthesized, and its performance was investigated in the degradation of organic pollutants (2,4-D and Mecoprop-P) in Killlex^R, BSA protein, and SARS-CoV-2 spike protein) and the disinfection of WWTP secondary effluent, using a narrowband low-energy visible light source (royal blue LED at 460 nm). The results from this study highlight the following:

- Similar degradation rates and percentage removal visible light irradiation were observed for 2,4-D and Mecoprop-P.
- The degradation performance of a photocatalyst is dependent on the available surface area for absorption for photocatalytic activity and the bond energies of the chemical bonds that exist in the contaminant.
- Released Ag^+ and CrO_4^{2-} from the GCN/ Ag_2CrO_4 nanocomposite were largely responsible for the BSA degradation and *cATP* reduction.
- Generated ROS were largely responsible for the disinfection of total coliforms and *E. coli*.
- The lower percentage degradation (70%) of SARS-CoV-2 spike protein can be attributed to its large molecular weight and structure compared to BSA protein.
- The pathways for degradation of proteins and the disinfection of microorganisms depend on any of the following: (1) binding affinity of the released metal ions from GCN/ Ag_2CrO_4 with the functional groups of proteins and *ATP*, (2) amount of ROS generated, and (3) the quantum of emission light from the photocatalyst that is absorbed and quenched by the proteins because of the light-induced protein oxidation.
- Significant disinfection results observed in the reduction of microorganisms' *cATP*, total coliforms, and *E. coli* with GCN/ Ag_2CrO_4 are also due to the reduction of the released Ag^+ to AgNPs by bacteria which was accelerated by light irradiation.
- Over one log reduction of microorganisms' *cATP*, total coliforms, and *E. coli* in wastewater secondary effluent was achieved in 60 min.
- The combination of GCN/ Ag_2CrO_4 and the narrowband low-energy light (royal blue LED at peak wavelength = 460 nm) holds promise in that it can be used in the wastewater treatment plant to degrade multiple recalcitrant organic pollutants and inactivate microorganisms.

Author Contributions: Conceptualization, O.O.A., L.Y. and G.A.; methodology, O.O.A.; experimental design, O.O.A. and L.Y.; formal analysis, O.O.A. and L.Y.; investigation, O.O.A.; resources, G.A.; writing—original draft presentation, O.O.A.; writing—review & editing, L.Y., J.H., M.G.K., C.R.J.H., S.P. and G.A.; supervision, G.A.; project administration, L.Y.; funding acquisition, G.A. All authors have read and agreed to the published version of the manuscript.

Funding: This work was carried out with the support and funding of the Natural Sciences and Engineering Research Council of Canada (NSERC), account number 10029431 and Alberta Innovates under the CASBE program, account number 10035007.

Data Availability Statement: The data presented in this study are available on request from the corresponding author.

Acknowledgments: The authors gratefully acknowledge the funding support provided by Natural Sciences and Engineering Research of Canada (NSERC) and Alberta Innovates under the CASBE program. We thank Advancing Canadian Water Assets (ACWA) for providing the WWTP secondary effluent.

Conflicts of Interest: The authors declare no conflict of interest.

References

1. Jiang, Y.; Liu, Z.; Zeng, G.; Liu, Y.; Shao, B.; Li, Z.; Liu, Y.; Zhang, W.; He, Q. Polyaniline-Based Adsorbents for Removal of Hexavalent Chromium from Aqueous Solution: A Mini Review. *Environ. Sci. Pollut. Res.* **2018**, *25*, 6158–6174. [[CrossRef](#)] [[PubMed](#)]
2. Liu, Y.; Liu, Z.; Zeng, G.; Chen, M.; Jiang, Y.; Shao, B.; Li, Z.; Liu, Y. Effect of Surfactants on the Interaction of Phenol with Laccase: Molecular Docking and Molecular Dynamics Simulation Studies. *J. Hazard. Mater.* **2018**, *357*, 10–18. [[CrossRef](#)]
3. Liu, Y.; Liu, Z.; Huang, D.; Cheng, M.; Zeng, G.; Lai, C.; Zhang, C.; Zhou, C.; Wang, W.; Jiang, D.; et al. Metal or Metal-Containing Nanoparticle@MOF Nanocomposites as a Promising Type of Photocatalyst. *Coord. Chem. Rev.* **2019**, *388*, 63–78. [[CrossRef](#)]
4. Ahmadian-Fard-Fini, S.; Ghanbari, D.; Salavati-Niasari, M. Photoluminescence Carbon Dot as a Sensor for Detecting of Pseudomonas Aeruginosa Bacteria: Hydrothermal Synthesis of Magnetic Hollow NiFe_2O_4 -Carbon Dots Nanocomposite Material. *Compos. Part B Eng.* **2019**, *161*, 564–577. [[CrossRef](#)]

5. Mamba, G.; Mishra, A.K. Graphitic Carbon Nitride (g-C₃N₄) Nanocomposites: A New and Exciting Generation of Visible Light Driven Photocatalysts for Environmental Pollution Remediation. *Appl. Catal. B Environ.* **2016**, *198*, 347–377. [[CrossRef](#)]
6. Kashale, A.A.; Rasal, A.S.; Kamble, G.P.; Ingole, V.H.; Dwivedi, P.K.; Rajoba, S.J.; Jadhav, L.D.; Ling, Y.-C.; Chang, J.-Y.; Ghule, A.V. Biosynthesized Co-Doped TiO₂ Nanoparticles Based Anode for Lithium-Ion Battery Application and Investigating the Influence of Dopant Concentrations on Its Performance. *Compos. Part B Eng.* **2019**, *167*, 44–50. [[CrossRef](#)]
7. Liu, Z.; Shao, B.; Zeng, G.; Chen, M.; Li, Z.; Liu, Y.; Jiang, Y.; Zhong, H.; Liu, Y.; Yan, M. Effects of Rhamnolipids on the Removal of 2,4,2,4-Tetrabrominated Biphenyl Ether (BDE-47) by *Phanerochaete Chrysosporium* Analyzed with a Combined Approach of Experiments and Molecular Docking. *Chemosphere* **2018**, *210*, 922–930. [[CrossRef](#)]
8. Zhang, C.; Li, Y.; Shuai, D.; Shen, Y.; Xiong, W.; Wang, L. Graphitic Carbon Nitride (g-C₃N₄)-Based Photocatalysts for Water Disinfection and Microbial Control: A Review. *Chemosphere* **2019**, *214*, 462–479. [[CrossRef](#)]
9. Zhang, T.; Jiang, B.; Huang, Y. UV-Curable Photosensitive Silicone Resins Based on a Novel Polymerizable Photoinitiator and GO-Modified TiO₂ Nanoparticles. *Compos. Part B Eng.* **2018**, *140*, 214–222. [[CrossRef](#)]
10. Fu, H.; Pan, C.; Yao, W.; Zhu, Y. Visible-Light-Induced Degradation of Rhodamine B by Nanosized Bi₂WO₆. *J. Phys. Chem. B* **2005**, *109*, 22432–22439. [[CrossRef](#)]
11. Liu, S.; Tian, J.; Wang, L.; Luo, Y.; Sun, X. One-Pot Synthesis of CuO Nanoflower-Decorated Reduced Graphene Oxide and Its Application to Photocatalytic Degradation of Dyes. *Catal. Sci. Technol.* **2012**, *2*, 339–344. [[CrossRef](#)]
12. Bao, N.; Shen, L.; Takata, T.; Domen, K. Self-Templated Synthesis of Nanoporous CdS Nanostructures for Highly Efficient Photocatalytic Hydrogen Production under Visible Light. *Chem. Mater.* **2008**, *20*, 110–117. [[CrossRef](#)]
13. Izadifard, M.; Achari, G.; Langford, C. Application of Photocatalysts and LED Light Sources in Drinking Water Treatment. *Catalysts* **2013**, *3*, 726–743. [[CrossRef](#)]
14. Izadifard, M.; Langford, C.H.; Achari, G. Photocatalytic Dechlorination of PCB 138 Using Leuco-Methylene Blue and Visible Light; Reaction Conditions and Mechanisms. *J. Hazard. Mater.* **2010**, *181*, 393–398. [[CrossRef](#)]
15. Ghosh, J.P.; Langford, C.H.; Achari, G. Characterization of an LED Based Photoreactor to Degrade 4-Chlorophenol in an Aqueous Medium Using Coumarin (C-343) Sensitized TiO₂. *J. Phys. Chem. A* **2008**, *112*, 10310–10314. [[CrossRef](#)]
16. Malkhasian, A.Y.S.; Izadifard, M.; Achari, G.; Langford, C.H. Photocatalytic Degradation of Agricultural Antibiotics Using a UV-LED Light Source. *J. Environ. Sci. Health Part B* **2014**, *49*, 35–40. [[CrossRef](#)]
17. Langford, C.; Izadifard, M.; Radwan, E.; Achari, G. Some Observations on the Development of Superior Photocatalytic Systems for Application to Water Purification by the “Adsorb and Shuttle” or the Interphase Charge Transfer Mechanisms. *Molecules* **2014**, *19*, 19557–19572. [[CrossRef](#)]
18. Shi, L.; Liang, L.; Ma, J.; Wang, F.; Sun, J. Remarkably Enhanced Photocatalytic Activity of Ordered Mesoporous Carbon/g-C₃N₄ Composite Photocatalysts under Visible Light. *Dalton Trans.* **2014**, *43*, 7236–7244. [[CrossRef](#)]
19. Tanveer, M.; Cao, C.; Ali, Z.; Aslam, I.; Idrees, F.; Khan, W.S.; But, F.K.; Tahir, M.; Mahmood, N. Template Free Synthesis of CuS Nanosheet-Based Hierarchical Microspheres: An Efficient Natural Light Driven Photocatalyst. *CrystEngComm* **2014**, *16*, 5290. [[CrossRef](#)]
20. Adhikari, S.P.; Pant, H.R.; Kim, J.H.; Kim, H.J.; Park, C.H.; Kim, C.S. One Pot Synthesis and Characterization of Ag-ZnO/g-C₃N₄ Photocatalyst with Improved Photoactivity and Antibacterial Properties. *Colloids Surf. A Physicochem. Eng. Asp.* **2015**, *482*, 477–484. [[CrossRef](#)]
21. Akintunde, O.O.; Yu, L.; Hu, J.; Kibria, M.G.; Achari, G. Visible-Light Driven Photocatalytic Degradation of 4-Chlorophenol Using Graphitic Carbon Nitride-Based Nanocomposites. *Catalysts* **2022**, *12*, 281. [[CrossRef](#)]
22. Jourshabani, M.; Dominic, J.A.; Achari, G.; Shariatinia, Z. Synergetic Photocatalytic Ozonation Using Modified Graphitic Carbon Nitride for Treatment of Emerging Contaminants under UVC, UVA and Visible Irradiation. *Chem. Eng. Sci.* **2019**, *209*, 115181. [[CrossRef](#)]
23. Faisal, M.; Ismail, A.A.; Harraz, F.A.; Al-Sayari, S.A.; El-Toni, A.M.; Al-Assiri, M.S. Synthesis of Highly Dispersed Silver Doped G-C₃N₄ Nanocomposites with Enhanced Visible-Light Photocatalytic Activity. *Mater. Des.* **2016**, *98*, 223–230. [[CrossRef](#)]
24. Wang, D.; Duan, Y.; Luo, Q.; Li, X.; Bao, L. Visible Light Photocatalytic Activities of Plasmonic Ag/AgBr Particles Synthesized by a Double Jet Method. *Desalination* **2011**, *270*, 174–180. [[CrossRef](#)]
25. Wang, P.; Huang, B.; Qin, X.; Zhang, X.; Dai, Y.; Wei, J.; Whangbo, M.-H. Ag@AgCl: A Highly Efficient and Stable Photocatalyst Active under Visible Light. *Angew. Chem. Int. Ed.* **2008**, *47*, 7931–7933. [[CrossRef](#)]
26. Bi, Y.; Ouyang, S.; Umezawa, N.; Cao, J.; Ye, J. Facet Effect of Single-Crystalline Ag₃PO₄ Sub-Microcrystals on Photocatalytic Properties. *J. Am. Chem. Soc.* **2011**, *133*, 6490–6492. [[CrossRef](#)]
27. Liu, Y.; Yu, H.; Cai, M.; Sun, J. Microwave Hydrothermal Synthesis of Ag₂CrO₄ Photocatalyst for Fast Degradation of PCP-Na under Visible Light Irradiation. *Catal. Commun.* **2012**, *26*, 63–67. [[CrossRef](#)]
28. Xu, D.; Cao, S.; Zhang, J.; Cheng, B.; Yu, J. Effects of the Preparation Method on the Structure and the Visible-Light Photocatalytic Activity of Ag₂CrO₄. *Beilstein J. Nanotechnol.* **2014**, *5*, 658–666. [[CrossRef](#)]
29. Deng, J.; Liang, J.; Li, M.; Tong, M. Enhanced Visible-Light-Driven Photocatalytic Bacteria Disinfection by g-C₃N₄-AgBr. *Colloids Surf. B Biointerfaces* **2017**, *152*, 49–57. [[CrossRef](#)]
30. Ren, Y.; Zhao, Q.; Li, X.; Xiong, W.; Tade, M.; Liu, L. 2D Porous Graphitic C₃N₄ Nanosheets/Ag₃PO₄ Nanocomposites for Enhanced Visible-Light Photocatalytic Degradation of 4-Chlorophenol. *J. Nanopart. Res.* **2014**, *16*, 2532. [[CrossRef](#)]

31. Liu, Z.; Jiang, Y.; Liu, X.; Zeng, G.; Shao, B.; Liu, Y.; Liu, Y.; Zhang, W.; Zhang, W.; Yan, M.; et al. Silver Chromate Modified Sulfur Doped Graphitic Carbon Nitride Microrod Composites with Enhanced Visible-Light Photoactivity towards Organic Pollutants Degradation. *Compos. Part B Eng.* **2019**, *173*, 106918. [CrossRef]
32. Canada, H. Guidelines for Canadian Drinking Water Quality—Summary Table. Available online: <https://www.canada.ca/en/health-canada/services/environmental-workplace-health/reports-publications/water-quality/guidelines-canadian-drinking-water-quality-summary-table.html> (accessed on 30 June 2021).
33. 2,4-D Technical Fact Sheet. Available online: <http://npic.orst.edu/factsheets/archive/2,4-DTech.html> (accessed on 5 March 2022).
34. Canada, H. Re-Evaluation Note REV2016-08, Special Review of 2,4-D: Proposed Decision for Consultation. Available online: <https://www.canada.ca/en/health-canada/services/consumer-product-safety/pesticides-pest-management/public-consultations/re-evaluation-note/2016/special-review-2-4-d/document.html> (accessed on 2 April 2022).
35. Anderson, A.; Byrtus, G.; Thompson, J.; Humphries, D.; Hill, B.; Bilyk, M. Baseline Pesticide Data for Semi-Permanent Wetlands in the Aspen Parkland of Alberta—Open Government. Available online: <https://open.alberta.ca/publications/0778524426> (accessed on 2 April 2022).
36. Gray, N.F. *Drinking Water Quality*, 2nd ed.; Cambridge University Press: Cambridge, UK, 2008; p. 538.
37. Flox, C.; Garrido, J.A.; Rodríguez, R.M.; Cabot, P.-L.; Centellas, F.; Arias, C.; Brillas, E. Mineralization of Herbicide Mecoprop by Photoelectro-Fenton with UVA and Solar Light. *Catal. Today* **2007**, *129*, 29–36. [CrossRef]
38. WHO Coronavirus (COVID-19) Dashboard. Available online: <https://covid19.who.int> (accessed on 31 December 2021).
39. CDC National Wastewater Surveillance System. Available online: <https://www.cdc.gov/healthywater/surveillance/wastewater-surveillance/wastewater-surveillance.html> (accessed on 5 April 2022).
40. EPA. *Wastewater Technology Fact Sheet: Bacterial Source Tracking*; United States Environmental Protection Agency: Washington, DC, USA, 2002; 12p.
41. Yu, L.; Achari, G.; Langford, C.H. Design and Evaluation of a Novel Light-Emitting Diode Photocatalytic Reactor for Water Treatment. *J. Environ. Eng.* **2018**, *144*, 04018014. [CrossRef]
42. Radwan, E.K.; Yu, L.; Achari, G.; Langford, C.H. Photocatalytic Ozonation of Pesticides in a Fixed Bed Flow through UVA-LED Photoreactor. *Environ. Sci. Pollut. Res.* **2016**, *23*, 21313–21318. [CrossRef]
43. Yu, L.; Achari, G.; Langford, C.H. LED-Based Photocatalytic Treatment of Pesticides and Chlorophenols. *J. Environ. Eng.* **2013**, *139*, 1146–1151. [CrossRef]
44. Alenazi, D.A.K.; Aslam, M.; Chandrasekaran, S.; Soomro, M.T.; Ali, S.; Danish, E.Y.; Ismail, I.M.I.; Hameed, A. Facile Fabrication of MoO₃/g-C₃N₄ p-n Junction for Boosted Photocatalytic Elimination of 2,4-D under Natural Sunlight Exposure. *J. Environ. Chem. Eng.* **2021**, *9*, 106304. [CrossRef]
45. Zhong, J.; Jiang, H.; Wang, Z.; Yu, Z.; Wang, L.; Mueller, J.F.; Guo, J. Efficient Photocatalytic Destruction of Recalcitrant Micropollutants Using Graphitic Carbon Nitride under Simulated Sunlight Irradiation. *Environ. Sci. Ecotechnol.* **2021**, *5*, 100079. [CrossRef]
46. Heydari, G.; Langford, C.H.; Achari, G. Passive Solar Photocatalytic Treatment of Emerging Contaminants in Water: A Field Study. *Catalysts* **2019**, *9*, 1045. [CrossRef]
47. Abubshait, S.A.; Iqbal, S.; Abubshait, H.A.; AlObaid, A.A.; Al-Muhimeed, T.I.; Abd-Rabboh, H.S.M.; Bahadur, A.; Li, W. Effective Heterointerface Combination of 1D/2D Co-NiS/S-g-C₃N₄ Heterojunction for Boosting Spatial Charge Separation with Enhanced Photocatalytic Degradation of Organic Pollutants and Disinfection of Pathogens. *Colloids Surf. A Physicochem. Eng. Asp.* **2021**, *628*, 127390. [CrossRef]
48. Iqbal, S.; Amjad, A.; Javed, M.; Alfakeer, M.; Mushtaq, M.; Rabea, S.; Elkaeed, E.B.; Pashameah, R.A.; Alzahrani, E.; Farouk, A.-E. Boosted Spatial Charge Carrier Separation of Binary ZnFe₂O₄/S-g-C₃N₄ Heterojunction for Visible-Light-Driven Photocatalytic Activity and Antimicrobial Performance. *Front. Chem.* **2022**, *10*, 975355. [CrossRef]
49. Baral, A.; Satish, L.; Das, D.P.; Sahoo, H.; Ghosh, M.K. Construing the Interactions between MnO₂ Nanoparticle and Bovine Serum Albumin: Insight into the Structure and Stability of a Protein–Nanoparticle Complex. *New J. Chem.* **2017**, *41*, 8130–8139. [CrossRef]
50. Huang, P.; Li, Z.; Hu, H.; Cui, D. Synthesis and Characterization of Bovine Serum Albumin-Conjugated Copper Sulfide Nanocomposites. *J. Nanomater.* **2010**, *2010*, 641545. [CrossRef]
51. Ballottin, D.; Fulaz, S.; Souza, M.L.; Corio, P.; Rodrigues, A.G.; Souza, A.O.; Gaspari, P.M.; Gomes, A.F.; Gozzo, F.; Tasic, L. Elucidating Protein Involvement in the Stabilization of the Biogenic Silver Nanoparticles. *Nanoscale Res. Lett.* **2016**, *11*, 313. [CrossRef] [PubMed]
52. Banerjee, V.; Das, K.P. Interaction of Silver Nanoparticles with Proteins: A Characteristic Protein Concentration Dependent Profile of SPR Signal. *Colloids Surf. B Biointerfaces* **2013**, *111*, 71–79. [CrossRef] [PubMed]
53. What Is the Difference Between Ordinary Light and Laser Light? Available online: <https://www.aydinlatma.org/en/what-is-the-difference-between-ordinary-light-and-laser-light.html> (accessed on 7 May 2022).
54. Kędziora, A.; Speruda, M.; Krzyżewska, E.; Rybka, J.; Łukowiak, A.; Bugła-Płoskońska, G. Similarities and Differences between Silver Ions and Silver in Nanoforms as Antibacterial Agents. *Int. J. Mol. Sci.* **2018**, *19*, 444. [CrossRef]
55. Djebbar, K.; Zertal, A.; Sehili, T. Photocatalytic Degradation of 2,4-Dichlorophenoxyacetic Acid and 4-Chloro-2-Methylphenoxyacetic Acid in Water by Using TiO₂. *Environ. Technol.* **2006**, *27*, 1191–1197. [CrossRef]

56. Helz, G.R.; Zepp, R.G.; Crosby, D.G. (Eds.) *Aquatic and Surface Photochemistry*; Lewis Publishers: Boca Raton, FL, USA, 1994; ISBN 978-0-87371-871-4.
57. Kumar, A.; Sharma, G.; Naushad, M.; Al-Muhtaseb, A.H.; Kumar, A.; Hira, I.; Ahamad, T.; Ghfar, A.A.; Stadler, F.J. Visible Photodegradation of Ibuprofen and 2,4-D in Simulated Waste Water Using Sustainable Metal Free-Hybrids Based on Carbon Nitride and Biochar. *J. Environ. Manag.* **2019**, *231*, 1164–1175. [[CrossRef](#)]
58. Ejeta, S.Y.; Imae, T. Photodegradation of Pollutant Pesticide by Oxidized Graphitic Carbon Nitride Catalysts. *J. Photochem. Photobiol. A Chem.* **2021**, *404*, 112955. [[CrossRef](#)]
59. Gu, J.; Chen, H.; Jiang, F.; Wang, X.; Li, L. All-Solid-State Z-Scheme Co₉S₈/Graphitic Carbon Nitride Photocatalysts for Simultaneous Reduction of Cr(VI) and Oxidation of 2,4-Dichlorophenoxyacetic Acid under Simulated Solar Irradiation. *Chem. Eng. J.* **2019**, *360*, 1188–1198. [[CrossRef](#)]
60. Zhong, J.; Ahmed, Y.; Carvalho, G.; Wang, Z.; Wang, L.; Mueller, J.F.; Guo, J. Simultaneous Removal of Micropollutants, Antibiotic Resistant Bacteria, and Antibiotic Resistance Genes Using Graphitic Carbon Nitride under Simulated Solar Irradiation. *Chem. Eng. J.* **2021**, *433*, 133839. [[CrossRef](#)]
61. General Chemistry. 2022. 1417.
62. Shi, T.; Wei, Q.; Wang, Z.; Zhang, G.; Sun, X.; He, Q.-Y. Photocatalytic Protein Damage by Silver Nanoparticles Circumvents Bacterial Stress Response and Multidrug Resistance. *MSphere* **2019**, *4*, e00175-19. [[CrossRef](#)] [[PubMed](#)]
63. Suryawanshi, V.D.; Walekar, L.S.; Gore, A.H.; Anbhule, P.V.; Kolekar, G.B. Spectroscopic Analysis on the Binding Interaction of Biologically Active Pyrimidine Derivative with Bovine Serum Albumin. *J. Pharm. Anal.* **2016**, *6*, 56–63. [[CrossRef](#)]
64. Jaiswal, V.D.; Dongre, P.M. Biophysical Interactions between Silver Nanoparticle-Albumin Interface and Curcumin. *J. Pharm. Anal.* **2020**, *10*, 164–177. [[CrossRef](#)] [[PubMed](#)]
65. Ershov, V.; Tarasova, N.; Ershov, B. Evolution of Electronic State and Properties of Silver Nanoparticles during Their Formation in Aqueous Solution. *Int. J. Mol. Sci.* **2021**, *22*, 10673. [[CrossRef](#)] [[PubMed](#)]
66. Klueh, U.; Wagner, V.; Kelly, S.; Johnson, A.; Bryers, J.D. Efficacy of Silver-Coated Fabric to Prevent Bacterial Colonization and Subsequent Device-Based Biofilm Formation. *J. Biomed. Mater. Res.* **2000**, *53*, 621–631. [[CrossRef](#)]
67. Dakal, T.C.; Kumar, A.; Majumdar, R.S.; Yadav, V. Mechanistic Basis of Antimicrobial Actions of Silver Nanoparticles. *Front. Microbiol.* **2016**, *7*, 1831. [[CrossRef](#)]
68. Rai, M.K.; Deshmukh, S.D.; Ingle, A.P.; Gade, A.K. Silver Nanoparticles: The Powerful Nanoweapon against Multidrug-Resistant Bacteria: Activity of Silver Nanoparticles against MDR Bacteria. *J. Appl. Microbiol.* **2012**, *112*, 841–852. [[CrossRef](#)]
69. Franci, G.; Falanga, A.; Galdiero, S.; Palomba, L.; Rai, M.; Morelli, G.; Galdiero, M. Silver Nanoparticles as Potential Antibacterial Agents. *Molecules* **2015**, *20*, 8856–8874. [[CrossRef](#)]
70. Zaheer, Z.; Kosa, S.A.; Akram, M. Interactions of Ag⁺ Ions and Ag-Nanoparticles with Protein. A Comparative and Multi Spectroscopic Investigation. *J. Mol. Liq.* **2021**, *335*, 116226. [[CrossRef](#)]
71. Jaiswar, A.; Varshney, D.; Adholeya, A.; Prasad, P. Do Environmentally Induced DNA Variations Mediate Adaptation in *Aspergillus Flavus* Exposed to Chromium Stress in Tannery Sludge? *BMC Genomics* **2018**, *19*, 868. [[CrossRef](#)] [[PubMed](#)]
72. Zhang, X.; Yang, C.-W.; Yu, H.-Q.; Sheng, G.-P. Light-Induced Reduction of Silver Ions to Silver Nanoparticles in Aquatic Environments by Microbial Extracellular Polymeric Substances (EPS). *Water Res.* **2016**, *106*, 242–248. [[CrossRef](#)] [[PubMed](#)]
73. Feng, T.; Liang, J.; Ma, Z.; Li, M.; Tong, M. Bactericidal Activity and Mechanisms of BiOBr-AgBr under Both Dark and Visible Light Irradiation Conditions. *Colloids Surf. B Biointerfaces* **2018**, *167*, 275–283. [[CrossRef](#)]
74. Zhu, L.; He, C.; Huang, Y.; Chen, Z.; Xia, D.; Su, M.; Xiong, Y.; Li, S.; Shu, D. Enhanced Photocatalytic Disinfection of *E. coli* 8099 Using Ag/BiOI Composite under Visible Light Irradiation. *Sep. Purif. Technol.* **2012**, *91*, 59–66. [[CrossRef](#)]
75. Ma, S.; Zhan, S.; Xia, Y.; Wang, P.; Hou, Q.; Zhou, Q. Enhanced Photocatalytic Bactericidal Performance and Mechanism with Novel Ag/ZnO/g-C₃N₄ Composite under Visible Light. *Catal. Today* **2019**, *330*, 179–188. [[CrossRef](#)]
76. Hatchard, C.G.; Parker, C.A.; Bowen, E.J. A New Sensitive Chemical Actinometer—II. Potassium Ferrioxalate as a Standard Chemical Actinometer. *Proc. R. Soc. Lond. Ser. A. Math. Phys. Sci.* **1956**, *235*, 518–536. [[CrossRef](#)]
77. Watanabe, K.; Matsuda, S.; Cuevas, C.A.; Saiz-Lopez, A.; Yabushita, A.; Nakano, Y. Experimental Determination of the Photooxidation of Aqueous I[−]—As a Source of Atmospheric I₂. *ACS Earth Space Chem.* **2019**, *3*, 669–679. [[CrossRef](#)]
78. Quick Start™ Bradford Protein Assay. Available online: <https://www.bio-rad.com/en-ca/product/quick-start-bradford-protein-assay?ID=5ec149ee-0cd1-468b-8651-a2fe9de6944d> (accessed on 19 June 2022).
79. Whalen, P. *Cellular Adenosine Triphosphate (CATP) Assay Procedure*; LuminUltra Technologies Ltd.: Fredericton, NB, Canada, 2012.
80. Colilert—IDEXX, US. Available online: <https://www.idexx.com/en/water/water-products-services/colilert/> (accessed on 19 June 2022).